Modified error in constitutive equations (MECE) approach for ultrasound elastography

Susanta Ghosh, Zilong Zou, Olalekan Babaniyi, Wilkins Aquino, Manuel I. Diaz, Mahdi Bayat, and Mostafa Fatemi

Citation: The Journal of the Acoustical Society of America **142**, 2084 (2017); doi: 10.1121/1.5006911
View online: https://doi.org/10.1121/1.5006911
View Table of Contents: http://asa.scitation.org/toc/jas/142/4
Published by the Acoustical Society of America

Modified error in constitutive equations (MECE) approach for ultrasound elastography

Susanta Ghosh, Zilong Zou, Olalekan Babaniyi,[a] Wilkins Aquino, and Manuel I. Diaz
Department of Civil and Environmental Engineering, Duke University, Durham, North Carolina 27708, USA

Mahdi Bayat and Mostafa Fatemi
Department of Physiology and Biomedical Engineering, Mayo College of Medicine, Rochester, Minnesota 55902, USA

(Received 7 May 2017; revised 23 August 2017; accepted 26 September 2017; published online 16 October 2017)

A partial differential equation-constrained optimization approach is presented for reconstructing mechanical properties (e.g., elastic moduli). The proposed method is based on the minimization of an error in constitutive equations functional augmented with a least squares data misfit term referred to as MECE for "modified error in constitutive equations." The main theme of this paper is to demonstrate several key strengths of the proposed method on experimental data. In addition, some illustrative examples are provided where the proposed method is compared with a common shear wave elastography (SWE) approach. To this end, both synthetic data, generated with transient finite element simulations, as well as ultrasonically tracked displacement data from an acoustic radiation force (ARF) experiment are used in a standard elasticity phantom. The results indicate that the MECE approach can produce accurate shear modulus reconstructions with significantly less bias than SWE. © *2017 Acoustical Society of America*. https://doi.org/10.1121/1.5006911

[GH] Pages: 2084–2093

I. INTRODUCTION

Elastography has gained high prominence in recent years as an imaging technique for non-invasive tissue characterization as mechanical properties have proven to be strong differentiators of disease. Techniques for elastography can be divided into quasi-static methods, in which inertial effects can be ignored due to the slow source application (Ophir, 1991), and transient methods in which propagating waves are used to reconstruct spatially varying properties (Krouskop *et al.*, 1987; Muthupillai *et al.*, 1995; Laurent *et al.*, 2002). Many of the existing techniques in transient elastography assume planar shear-dominated waves propagating in an infinite medium. The latter assumptions lead to straightforward formulas for computing local shear wave speeds from time-of-travel measurements across a grid of points (Bercoff, 2004; Nightingale, 2003; Song *et al.*, 2012).

From the clinical point of view, ultrasound shear wave elastography (SWE) holds the potential for diagnosis of many diseases, including detection of malignant masses (e.g., breast, thyroid) and assessing fibrosis in liver. Meanwhile, investigations for other clinical applications are rapidly increasing. In particular, SWE is a valuable and promising tool for improving the sensitivity and specificity for breast cancer detection (Berg *et al.*, 2012; Athanasiou *et al.*, 2010; Cosgrove *et al.*, 2012; Bayat *et al.*, 2017; Denis *et al.*, 2016). SWE methods are very attractive from the practical point of view as they are very simple to implement and computations can be carried out in near real-time. The main drawback of these methods is that their underlying assumptions (e.g., plane waves in an unbounded domain) can be easily violated in practical cases, leading to undesirable artifacts in the reconstructed images (Nightingale, 2003) or a biased estimation of modulus (Zhao *et al.*, 2011).

Partial differential equation (PDE)-based approaches relax the underlying assumptions of planar waves and unbounded domains and, hence, can handle general waveforms, heterogenous media, and general boundary conditions (Feissel and Olivier, 2007; Banerjee *et al.*, 2013; Diaz *et al.*, 2015). The main component is that they work with a general elastic or viscoelastic initial-boundary-value problem (i.e., wave equation plus initial conditions and boundary conditions). These methods can be classified into direct and iterative approaches. Direct approaches usually need full field data (i.e., displacements measured in all dimensions at all points in the domain) and can produce a linear system of equations or even a decoupled and local set of equations that can be solved in one step. For instance, algebraic direct inversion (Oliphant *et al.*, 2001; Sinkus *et al.*, 2005; Park and Maniatty, 2006) falls in the latter category, while a more recent method in the former category is the adjoint weighted equations approach (Albocher *et al.*, 2009). The main advantage of direct inversion methods is that a single solution of a system of equations is usually needed, while handling very general geometries and boundary conditions. Their main drawbacks are the need for full field measurements and their sensitivity to noise due to the presence of measurement derivatives in the formulations.

Iterative approaches commonly arise when the inverse problem is postulated within a general nonlinear optimization framework. The advantage of these approaches is that full field measurements are not needed, but at the expense of increased computational cost as boundary-value problems

[a]Electronic mail: lekanbg@gmail.com

 0001-4966/2017/142(4)/2084/10/$30.00

have to be solved repeatedly during the optimization process. However, an attractive feature of optimization-based approaches is that noise can be readily handled. Some recent examples of optimization-based strategies can be found here (Doyley *et al.*, 2000; Oberai *et al.*, 2003; Feissel and Olivier, 2007; Brigham *et al.*, 2007; Aguilo *et al.*, 2010). Some of the limitations of existing optimization-based approaches include the need to specify boundary conditions, sensitivity to initial guess, and computational expense. Our aim is to devise an iterative strategy that circumvents these drawbacks, but still offers the generality of optimization-based strategies.

Our main contribution in this work is an ultrasound-based elastography strategy that can handle general waveforms, geometries, boundary conditions, and sparse data (unidirectional fields). To this end, our framework consists of two components: (1) acoustic radiation force excitation and ultrasound-based wave tracking, and (2) a novel modified error in constitutive equation (MECE) approach for inverting for shear modulus. The MECE approach uses a combination of energy-based and displacement-based functionals as the objective to be minimized in an optimization problem (Feissel and Olivier, 2007; Banerjee *et al.*, 2013). One of the salient features of the MECE approach is that besides incorporating measured data in the objective, it also incorporates an error in the constitutive equations, adding a strong physical sense to the framework. The MECE approach was first used for elasticity imaging problems in (Banerjee *et al.*, 2013) and was extended to elasticity imaging in coupled acoustic-structure systems (Warner *et al.*, 2014).

One of the most attractive features for using MECE in elastography is the fact that unknown boundary conditions (i.e., tractions and/or displacements) can be naturally handled (Diaz *et al.*, 2015). That is, the formulation allows for problems where the boundary conditions are partially or completely unknown and the data set is available only on a portion of the body under investigation. In other words, the methodology allows us to isolate regions of interest (ROI) where ultrasound data is available and perform inversions in these local subdomains. We demonstrate in the present work that different subregions of the same body can be imaged simultaneously using our proposed approach. Furthermore, we demonstrate that the penalty term that appears in MECE can be adapted to address the levels of noise present in ultrasound data. The MECE approach has been extensively studied numerically, but no studies have been reported on its performance with real experimental data. Therefore, we offer a detailed experimental study in which we interrogated a laboratory phantom using different configurations of acoustic radiation force excitation. The ensuing displacement fields were used with MECE to estimate shear modulus distribution over different regions of the phantom. To the best knowledge of the authors, this is the first experimental study that demonstrates the feasibility of using MECE in ultrasound-based elasticity imaging.

There have been few studies that compare the performance of local SWE approaches with optimization-based techniques. A recent contribution in this direction can be found in the work of Arnal *et al.* (2013). These researchers performed a detailed study in which they compared a least-squares full-wave inversion approach to SWE. They used a scalar acoustics equation, as opposed to the full elasticity equations used in the present work, and showed that full-wave inversion can provide improved shear modulus reconstructions when compared to local shear wave imaging methods. In a similar fashion, we provide an illustrative comparison of the performance of our MECE approach and a common SWE algorithm using simulated and experimental phantom data.

The rest of the paper is organized as follows. We first describe the theoretical background of the MECE optimization technique and a conventional SWE method in Secs. II and III, respectively. We then perform a simulation experiment in Sec. IV to compare the MECE approach to the SWE method. In Sec. V A, we provide details of the experiments conducted in this work. Then, the study proceeds with applying MECE and SWE toward estimating the shear modulus distribution from the experimental measurements in Sec. V B. We provide conclusions and future directions in Sec. VI.

II. THEORETICAL BACKGROUND: THE MECE APPROACH

In this section, we provide a brief summary of the MECE approach as applied to the elasticity imaging problem (Banerjee *et al.*, 2013; Warner *et al.*, 2014; Diaz *et al.*, 2015). In particular, we present a recently developed version of MECE in which boundary conditions can be partially known or completely unknown (Diaz *et al.*, 2015). The latter is an attractive feature for material property inversion using ultrasound data. We also provide a description for the SWE algorithm used in this work.

A. Governing equations

We will describe the motion of tissue in the frequency-domain. To this end, the governing elastodynamics equation is

$$\nabla \cdot \boldsymbol{\sigma} + \rho\omega^2 \boldsymbol{u} = 0 \qquad \text{in}\,\Omega, \tag{1}$$

where $\boldsymbol{u}$ is the displacement field, ω is the angular frequency, ρ denotes the mass density, and $\boldsymbol{\sigma}$ is the stress tensor. The problem domain is denoted as Ω and its boundary as Γ. Notice that we have not specified any conditions on the boundary Γ, which renders the forward elastodynamics problem ill-posed in the absence of any additional information. This lack of boundary information can be handled naturally by the MECE formulation as shown in (Diaz *et al.*, 2015).

We will use the following definitions and decompositions for strains and stresses.

$$\boldsymbol{\epsilon}[\boldsymbol{u}] := \frac{1}{2}(\nabla \boldsymbol{u} + \nabla \boldsymbol{u}^T), \tag{2a}$$

$$e_u := \mathrm{tr}(\boldsymbol{\epsilon}[\boldsymbol{u}]), \tag{2b}$$

$$\boldsymbol{\epsilon}_{\mathrm{dev}}[\boldsymbol{u}] := \boldsymbol{\epsilon}[\boldsymbol{u}] - \frac{1}{3} e_u \boldsymbol{I}, \tag{2c}$$

$$p := \frac{1}{3}\mathrm{tr}(\boldsymbol{\sigma}), \tag{2d}$$

$$\boldsymbol{\sigma}_{\mathrm{dev}} := \boldsymbol{\sigma} - p\,\boldsymbol{I}. \tag{2e}$$

In these expressions, $\boldsymbol{I}$ is the second-order identity tensor, e_u is the volumetric strain, $\boldsymbol{\epsilon}_{\mathrm{dev}}[\boldsymbol{u}]$ is the deviatoric strain tensor, $\boldsymbol{\sigma}_{\mathrm{dev}}$ is the deviatoric stress tensor, and p is the mean stress or pressure. At this point in our formulation, we do not specify the constitutive relationship between stress and strain tensors. These relationships will arise naturally in the MECE context through a minimization problem as presented in Sec. II B.

In this work, we focus on compressible, isotropic, elastic materials. These materials can be characterized by two elastic constants: the bulk modulus, B, and the shear modulus, G. Soft biological tissue is nearly incompressible. Therefore, we will take the bulk modulus as known and equal to that of water. In this case, only the shear modulus component of the constitutive equations will be treated as an unknown in the derivations presented herein.

B. Inverse problem formulation

We denote $\tilde{\boldsymbol{d}}$ as the measured displacements defined over a set $\Omega_{\mathrm{m}} \subseteq \Omega$. The elastography inverse problem can be concisely described as finding the fields $\boldsymbol{u}$, $\boldsymbol{\sigma}$, and G that are, in some sense, in agreement with the measured displacements and that also satisfy Eq. (1).

We formulate the inverse problem as a nonlinear PDE constrained optimization problem. The objective functional is defined as

$$\Lambda(\boldsymbol{u},\boldsymbol{\sigma},G) := U(\boldsymbol{u},\boldsymbol{\sigma},G) + \frac{\kappa}{2}\int_{\Omega_{\mathrm{m}}} (\boldsymbol{u}-\tilde{\boldsymbol{d}})\cdot\mathbf{T}(\boldsymbol{u}-\tilde{\boldsymbol{d}})d\Omega, \tag{3}$$

where

$$U(\boldsymbol{u},\boldsymbol{\sigma},G) := \frac{1}{2}\int_{\Omega}\frac{1}{2G}\|\boldsymbol{\sigma}_{\mathrm{dev}} - 2G\,\boldsymbol{\epsilon}_{\mathrm{dev}}[\boldsymbol{u}]\|^2\,\mathrm{d}V + \frac{1}{2}\int_{\Omega}\frac{1}{B}(p - Be_u)^2\,\mathrm{d}V.$$

In the above expressions, $\kappa > 0$ is a parameter that can be used to adjust how closely the measured data is approximated. The variable $\mathbf{T}$ denotes an observation tensor that can be used to capture measured components of the displacement field. Conventional ultrasound imaging has poor accuracy in the estimation of lateral displacements. This is especially true in the case of small lateral displacements excited with an acoustic radiation force. In addition, acoustic radiation forces are mostly aligned with the ultrasound beam direction, hence, in homogeneous areas, lateral motions are significantly smaller than axial displacements. The tensor $\mathbf{T}$ is used to account for this preferential directionality in the data.

We cast our optimization problem as

$$(\boldsymbol{u}_*,\boldsymbol{\sigma}_*,G_*) := \underset{\boldsymbol{u}\in\mathcal{U},\boldsymbol{\sigma}\in\mathcal{S}(\boldsymbol{u}),G\in\mathcal{Z}}{\arg\min}\ \Lambda(\boldsymbol{u},\boldsymbol{\sigma},G), \tag{4}$$

where $\mathcal{U}$ is an admissible space of displacements, $\mathcal{S}(\boldsymbol{u})$ is an admissible space of stresses (i.e., symmetric tensors), and $\mathcal{Z}$ is an admissible space of shear modulus (i.e., positive and bounded). We find this minimum in practice by first stating optimality conditions using Lagrange multipliers and taking directional derivatives of the ensuing Lagrangian. Setting these derivatives to zero, we obtain a nonlinear system of equations that are then discretized with the Finite Element Method, and solved with an alternating directions minimization strategy as shown in (Banerjee *et al.*, 2013; Warner *et al.*, 2014; Diaz *et al.*, 2015).

We would like to remark some of the salient features of the MECE formulation presented in Eqs. (3) and (4). Since this type of formulation is not widely known, it is important to point out some of the reasons for our choice. Notice that in this formulation the constitutive equations are relaxed by incorporating them in the objective functional Eqs. (3). One interpretation for this objective is that we are willing to accept a residual error at the end of the minimization process in the equations that connect stresses and strains. After all, we are trying to estimate parameters in these relations using imperfect data and imperfect models. This relaxation is (at least in part) responsible for the improved convexity of the problem reported in (Feissel and Olivier, 2007). Improved convexity translates into robustness with respect to initial guesses and not getting trapped in local minima. Another important advantage of MECE formulations that was first put forward in (Diaz *et al.*, 2015) is the possibility of not specifying boundary conditions as part of the PDE constraints. Notice that when working with interior data, such as that coming from ultrasound tracking, the data on the boundary of the region of interest is noisy and unidirectional. Therefore, this data usually cannot be used as known boundary conditions. The aforementioned features make MECE formulations very attractive for parameter identification problems in general.

C. Determining parameters in the data misfit term

In a MECE formulation, it is very important to devise a sound strategy to select the parameter κ that appears in the data misfit term. We recall that this term regulates how strongly the displacement predicted by the model matches the measurements, and how well the constitutive equation is satisfied. To this end, we used the error balance technique that was first proposed in (Warner *et al.*, 2014). We do not elaborate further on this topic as the details are outside the scope of this paper. We provide some details on the weighting tensor, $\mathbf{T}$, in the Appendix.

III. SHEAR WAVE ELASTOGRAPHY (SWE) APPROACH

We now briefly describe a shear wave elastography (SWE) procedure that will be used for comparison with our MECE approach. In SWE, the local speed of shear waves is related to the shear modulus under the assumption of a plane wave propagating in an infinite medium. Hence, measurement of the wave speed is the first step in this method. Usually, a time-of-flight technique is used for local speed calculations. In this approach, for each point in the imaging

domain, a limited area is selected and based on a presumed wave direction, time traces from adjacent points located at a known distance, Δx, along the wave trajectory are compared to find a time delay, Δt. The wave speed, c_s, is then calculated as $c_s = \Delta x/\Delta t$.

To enhance the estimation of time delays, several steps of signal conditioning are added to enforce spectral and temporal constraints based on the choice of excitation method (e.g., acoustic radiation force or external mechanical shaker). For example, frequency components outside the desired bandwidths are removed using band-pass filtering and time windowing may be used to enforce zero displacement at the beginning and the end of the wave observation window (Song *et al.*, 2012).

For shear wave reconstruction in this paper, the displacement data was first filtered using a band-pass filter with an effective bandwidth between 65–500 Hz followed by a time-domain Tukey window with a parameter equal to 0.25. A problem that arises in the time-of-flight approaches is the lack of knowledge about wave trajectory *a priori*. To tackle this problem, a method based on a two-dimensional search is presented in (Song *et al.*, 2014) which allows for estimation of the shear wave speed propagating in an arbitrary angle in the imaging plane. The latter method was adapted here for the reconstruction of the shear wave maps.

IV. RECONSTRUCTION WITH SIMULATED DATA: COMPARISON OF SWE AND MECE

A. Methodology

In this section, we present a set of problems in which inversions were carried out using simulated data with both our MECE algorithm and a conventional SWE approach. Before proceeding with an experimental protocol to validate our MECE strategy, we investigated the relative merits of using a PDE-constrained optimization approach for elastography as opposed to simpler and computationally faster approaches such as SWE.

We used two different domains for our study as shown in Fig. 1. Both domains had dimensions 0.2 m × 0.2 m. One domain consisted of a soft matrix with a cylindrical inclusion, while the other domain had the same matrix background with a triangular inclusion. We expected that a triangular inclusion would be more challenging to SWE approaches due to strong wave diffraction. The shear modulus of the background material in both cases was taken as 5 kPa, while the shear modulus of the inclusions was 25 kPa. The density of the background and inclusions in both cases was taken as 1000 kg/m^3. Similarly, the bulk modulus for inclusions and matrix was considered known with a value of 1 MPa. Other relevant parameters for the simulation are reported in Table I.

We used two dimensional (2D) transient finite element simulations to produce synthetic data from which we inverted for shear modulus distributions using both our MECE approach and the SWE technique described in Sec. III. A shear traction was applied on the middle of the right side of the domain (see Fig. 1), and the rest of the sides were modeled as fixed or free. The applied traction was a half sine wave with total duration of 7.45 ms. To generate the synthetic data, we used very refined finite element discretizations conforming to the geometry of the inclusions (i.e., irregular meshes). For the inversion, the displacement fields were interpolated onto a different, rectangular (regular) grid with nodal spacing of 1.5 mm × 1.5 mm for the cylindrical inclusion, and 0.75 mm × 0.6 mm for the triangular inclusion. For the MECE algorithm, a fast Fourier transform (FFT) was used to convert interpolated transient displacements to the frequency domain, and displacements at frequencies ranging from 3.26 to 146.48 Hz (with 12 frequencies in between) were used for the reconstructions. The interpolated, transient data was also used in the conventional SWE approach to estimate the modulus distribution.

Although we did not add random noise to the simulated data, it is important to recognize that the regular grid used for the reconstruction cannot reproduce the shapes of the inclusions exactly. Also, there is some numerical error due to the interpolation and transformation of the data from the time to the frequency domain. Since both algorithms are compared with the same data, the addition of random noise was not deemed necessary. Furthermore, we will present results with laboratory experiments in Sec. V, which contained real noise due to ultrasound tracking, modeling error, etc.

B. Cylindrical and triangular inclusion reconstructions

The reconstructions for both configurations are shown in Figs. 2 and 3. In both figures, we show the reconstruction from a conventional SWE algorithm, and reconstructions obtained using our MECE approach with full field displacement data (both u_x and u_z) and unidirectional displacement data (only u_z). Unidirectional data was used to simulate real

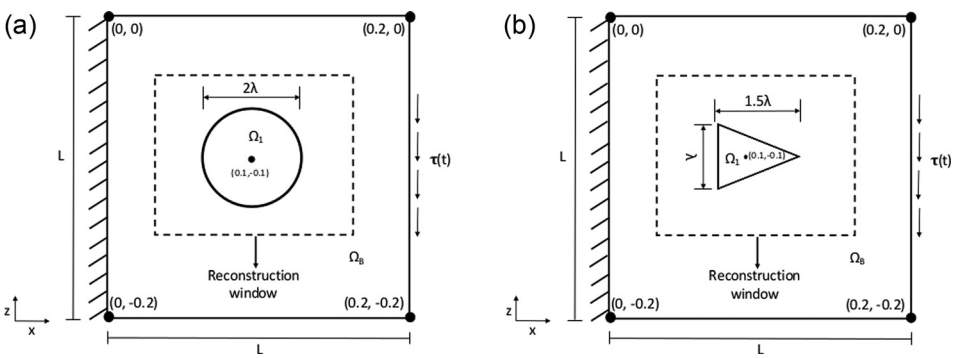

FIG. 1. Problem setup. The forward problem is solved in the full domain, while the inverse problem is solved only in the reconstruction window. The parameters for the problem are given in Table I. (a) Cylindrical inclusion. (b) Triangular inclusion.

TABLE I. Parameters for time domain forward problem for both the cylindrical and triangular inclusions. In the table $f(t) = 1$ for $t \leq 7.45$ ms. and $f(t) = 0$ for $t > 7.45$ ms.

Name	Value
Loading $\tau(t)$	$f(t)\sin(2\pi f_l t)$
f_l	67.08 Hz
L	0.2 m
λ	$\frac{1}{30}$ m
Background G	5 kPa
Inclusion G	25 kPa
B	1 MPa
Time step	3×10^{-4} s
Simulation duration	0.21 s

situations where the ultrasound system is only capable of measuring one component of the displacement field with high accuracy. In all cases, the MECE approach produced accurate location and size of the inclusions with very clear and sharp edges. The SWE algorithm also produced an accurate position of the inclusions for both cases, but with a more diffuse appearance of the edges. These diffuse edges are especially noticeable in the reconstruction for the triangular inclusion case.

To quantify the accuracy of the reconstructions, we computed the average shear modulus over the true position of the target inclusion, denoted by the white contours in Figs. 2 and 3. We then computed the error between the reconstructed shear modulus (SM) distribution and the reference with the formula

$$\text{Error} = \frac{\int_\Omega \mu_{\text{ref}} - \mu_{\text{rec}}\, d\Omega}{\int_\Omega \mu_{\text{ref}}\, d\Omega}, \tag{5}$$

where μ_{ref} is the reference SM distribution, and μ_{rec} is the reconstruction. These errors and the averages are reported in Table II. For the inclusion, the maximum error produced by the MECE approach was about 4% of the true value and occurred for the case with a triangular inclusion, while for the SWE algorithm the corresponding maximum error was about 38%. For the background material, the maximum relative error for the MECE approach was about 13% and occurred for the case with a cylindrical inclusion, while for the conventional SWE approach the maximum error was about 39% and occurred in the reconstruction of the triangular inclusion.

C. Findings and conclusions of simulated data experiments

From the simulation results, we see that the MECE approach is capable of producing more accurate reconstructions than SWE in the cases that we studied. One reason, among others, for this improved performance is the fact that some of the simplifying assumptions in SWE, such as plane wave propagation, lead to significant modeling errors, while in MECE we allow for general wave patterns. Moreover, since MECE is a full-wave inversion approach, the solution uses global information as opposed to local information, which was identified as one of the factors for improved reconstructions in the work of Arnal *et al.* (2013). We also observed that reconstructions obtained from full field data were more accurate than the ones obtained with unidirectional data, as expected. The latter results are consistent with findings reported in (Banerjee *et al.*, 2013; Diaz *et al.*, 2015).

V. RECONSTRUCTIONS WITH EXPERIMENTAL DATA

A. Experiments description

Acoustic radiation force experiments were performed on a standard tissue-mimicking elasticity phantom with cylindrical inclusions (CIRS model 049 A, CIRS, Norfolk, VA). The Young's modulus of the phantom background and inclusion was 25 and 80 kPa, respectively (type IV). The inclusion had a diameter of 10.404 mm and it was located 30 mm below the phantom surface. Acoustic attenuation was 0.5 dB/cm-MHz for both background and inclusion materials. A Verasonics programmable ultrasound machine (Verasonics Inc., Redmond, WA) with a linear array transducer (L11-4v, Verasonics, Kirkland, WA) was used for both imaging of the phantom and creation of the acoustic radiation force push beams.

Three experiments were conducted. In each experiment, a single ARF push was applied at a depth that was equivalent to the center of the inclusion, but at different locations (Fig. 4). Each push beam was sent at 4.09 MHz center frequency with 600 μs duration and 150 V peak-to-peak voltage. Fast

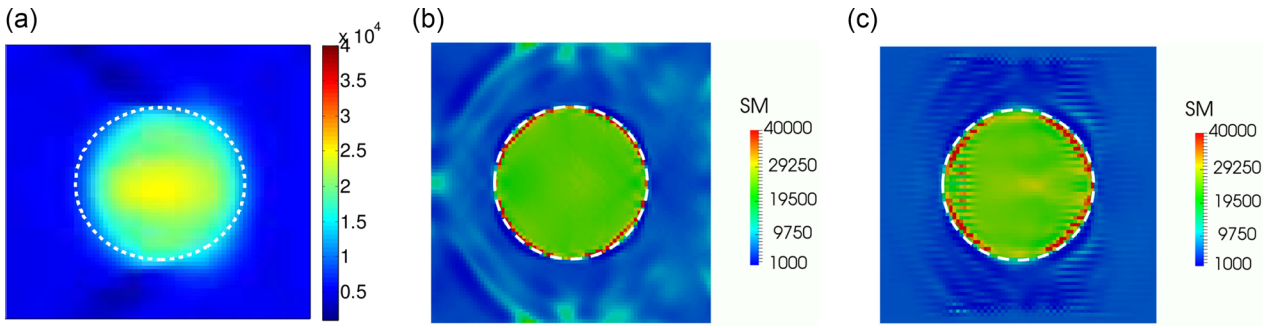

FIG. 2. (Color online) Shear modulus (SM) reconstruction for a cylindrical inclusion using an optimization formulation (MECE) and a conventional SWE method. The given values are in Pascals. The actual location of the inclusion boundary is indicated by the broken white curve. (a) SWE method. (b) MECE full field data. (c) MECE unidirectional data.

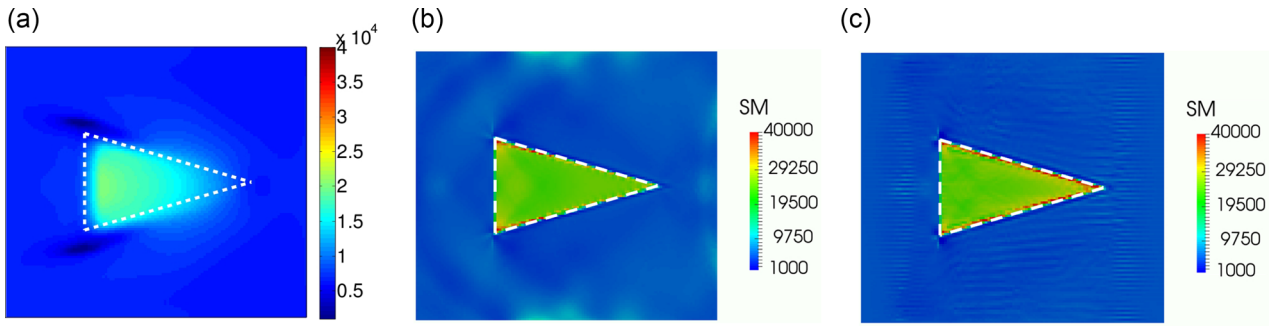

FIG. 3. (Color online) Shear modulus (SM) reconstruction for a triangular inclusion using MECE and a conventional SWE method. The SM values are in Pascals. The actual location of the inclusion boundary is indicated by the broken white curve. (a) SWE method. (b) MECE full field data. (c) MECE unidirectional data.

imaging at 4444 frames per second (fps) was performed immediately after application of the ARF pushes. The axial sampling was set to $\lambda/8$, while the lateral sampling was λ, where λ is the wavelength corresponding to the center frequency of the probe (6.25 MHz). The displacement was then calculated for each point inside of the imaging plane using the 2D autocorrelation technique (Loupas and Powers, 1995). Eight axial samples were then replaced by their average value to result in a uniformly sampled velocity map in both axial and lateral directions. A schematic of the phantom geometry and location of pushes is shown in Fig. 4.

B. Methodology

Now we present the reconstruction of shear modulus using the MECE algorithm (see Sec. I) with data from the laboratory experiments described in Sec. V A. We also present the SWE reconstruction of shear modulus, within the same ROI selected for MECE, for comparison purposes. The standard inclusion phantom used in our experimental studies provided details about the inclusion geometry and its location. We used this information to identify the location of inclusion in our reconstruction maps using a registered B-mode image (Fig. 5). The modulus values for inclusion and background were then acquired based on this segmentation.

1. MECE Data pre-processing

Before proceeding with the inversion, the time-domain experimental data was pre-processed as follows. In all cases, only the vertical component of the measured displacement fields was used. Since our formulation is in the frequency domain, the measured displacement time histories were Fourier transformed and only a small subset of the frequency spectra was used for inversion. The frequency spectra for the different experiments showed a common decreasing trend with frequency. We selected an upper bound of 694.4 Hz for the frequency of interest based on the energy content of the Fourier spectra. In all the experiments, seven frequencies were used ranging from 277.8 Hz to 694.4 Hz at an interval of 69.4 Hz. Again, these numbers were directly taken from the FFT results. The lower end frequency was selected as to always obtain at least one wavelength in any of the subdomains used for reconstruction.

TABLE II. Average shear modulus (SM) values in the inclusion (Incl.) and background (Bck.) regions for the simulation experiment. The errors between the reconstructed and reference SM values are also displayed on the table. The reference inclusion SM is 25 kPa, and the reference background SM is 5 kPa.

Inclusion Type	Method	Avg. SM in Incl. (kPa)	Avg. SM in Bck. (kPa)	Inclusion error (%)	Background error (%)
Cylinder	MECE, with u_x	24.9	5.42	0.400	8.40
	MECE, no u_x	25.5	4.36	2.00	12.8
	SWE	18.6	5.69	25.6	13.8
Triangle	MECE, with u_x	24.7	5.14	1.20	2.80
	MECE, no u_x	26.0	4.69	4.00	6.20
	SWE	15.5	6.95	38.0	39.0

2. MECE modeling assumptions

One important component of our reconstruction strategy is how to deal with the fact that ultrasound measurements are obtained on a plane whereas the actual geometry and wave propagation are three-dimensional. To address this issue we investigated two assumptions: (1) axisymmetry with the axis of symmetry coinciding with the axis of push,

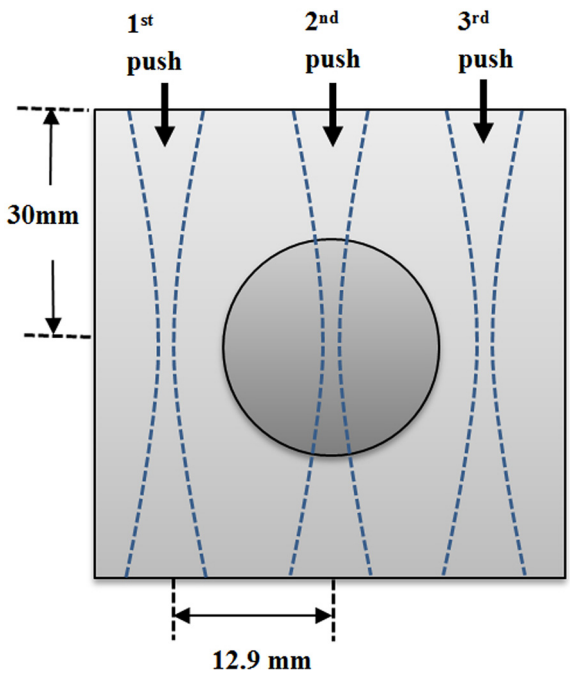

FIG. 4. (Color online) Phantom geometry and location of ARF pushes.

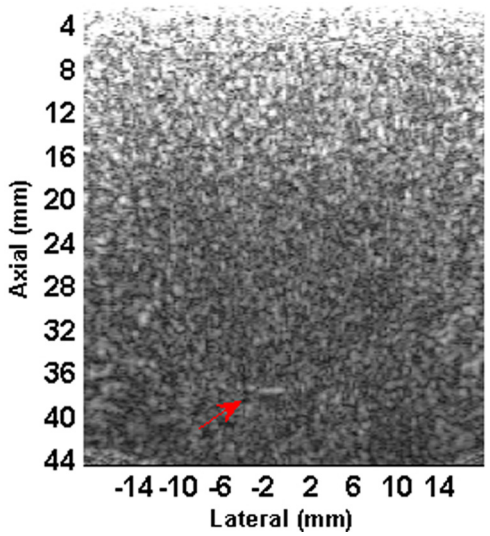

FIG. 5. (Color online) B-mode image. The inclusion does not provide a significant contrast compared to background. However, a partially visible part of the inclusion edge (arrow) was used to identify its location.

and (2) a plane strain condition in which displacements and strains out of the plane are taken as zero. Both these assumptions produced nearly identical results and were verified using numerical simulations. We found that the ensuing modeling errors were small compared to the noise contained in common ultrasound data. Hence, we arbitrarily chose the axisymmetric condition to proceed with our inversions. It is important to reiterate that the value of the bulk modulus for all materials was assumed to be the same as that of water (2.2 GPa), and hence only the shear modulus field was treated as unknown. In all cases, we used a mass density $\rho = 1000\,\mathrm{kg/m^3}$.

3. Region of interest (ROI) for inversion

One of the main advantages of our inversion formulation is that it allows for reconstructions within arbitrary subdomains selected from the plane of ultrasound measurements. These subdomains will be called computational domains from hereon and are shown in Fig. 6. Table III provides details on the sizes of these computational domains for the different experiments. The computational domains for experiments 1 to 3 were taken such that the axis of the acoustic radiation force was parallel to the vertical boundary and slightly outside of the ROI. We have deliberately kept the zone surrounding the push outside the computational since we did not include the radiation force in our formulation.

TABLE III. Finite element meshes used in the reconstructions.

		No. of elements		
Experiment No.	Domain size (mm)	Along X	Along Y	Total
1	25.3 × 31.43	230	100	23 000
2	10.9 × 31.43	110	100	11 000
3	24.8 × 31.43	230	100	23 000

4. Additional details on the MECE optimization process

The finite element meshes used in the inversion were selected such that the forward solution errors were low for the wavelengths observed in the experiments. That is, we performed convergence studies to ensure that the finite element computations were sufficiently accurate. The finite element meshes used were structured and consisted of four-node bilinear quadrilateral elements, see Table III for more details. The experimental data was interpolated onto the finite element meshes for the inversion process.

The initial guess was taken as a homogeneous material with a shear modulus of 500 Pa. We observed that the reconstructed shear modulus distribution remained almost insensitive to the choice of initial guess, which is a salient feature of the MECE formulation. The optimization algorithm was considered converged when the relative change in the MECE functional was smaller than 0.01 in two successive iterations. Our experience suggests that this tolerance should be sufficient in the current application, and further reducing the tolerance would not alter the reconstructed shear modulus distribution significantly.

5. SWE reconstruction

We used the reconstruction method described in Sec. III to create shear modulus maps within the same computational domains that were used for MECE.

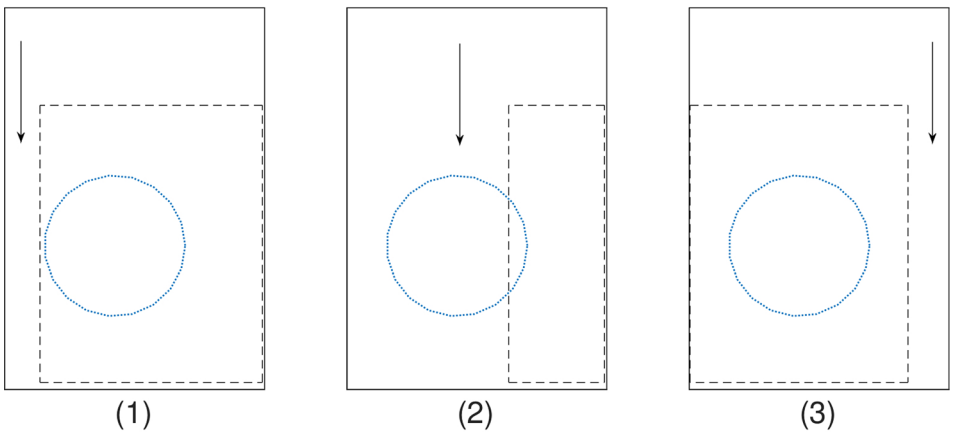

FIG. 6. (Color online) Sketches of the experimental and computational domains for experiments 1–3. AB is a horizontal line through the middle of the computational domain used in the results and discussions presented herein. The arrow indicates the location of the ARF push.

C. Results and discussion

In all the experiments, we evaluated the accuracy of the reconstructions by comparing their known values with the following two criteria: (1) geometry of the reconstructed inclusion, (2) the mean value of the shear modulus over the inclusion and background.

The MECE and SWE reconstructed shear modulus distributions are given in Fig. 7 for experiments 1–3. The position of the computational domain is represented by the colored image, while the experimental grid is denoted by the black surrounding box. The known boundary of the inclusion is sketched in this figure using a solid line.

From Fig. 7, we can see that the inclusion was accurately recovered in all cases in both MECE. Furthermore, notice that the results are consistent across all subdomains with respect to the position and shape of the inclusion. In addition, the boundary between the inclusion and the background is distinctly identified. As can be seen from the recovered images, the proposed MECE technique is amenable to reconstructions with data in domains of arbitrary size and shape. In particular for experiment 2, the shape, location and boundary of the inclusion is captured well despite the fact that only a small portion (of the inclusion) is present inside the computational domain. We would like to point out that there was no conditioning of the data (e.g., filtering) prior to the inversion with MECE. Although the solutions are oscillatory, the inclusion was clearly identified in all cases despite the fact that the latter is not visible in the B-mode image. The SWE reconstruction of modulus for different push location experiments are shown in Fig. 7. The general reconstruction features in terms of location and geometry are similar to those of MECE. However, reconstruction anomalies, such as unexpected modulus variations in background and inclusion areas, show features which are distinctly different from those of MECE. For example, dark bands (e.g., comet-tail trace) are observed within the background and near the edges of inclusion, distal to the location of the radiation force push.

Figure 8 shows the cross sectional plots of the reconstructed shear modulus distribution for experiments 1 to 3 along Line AB shown in Fig. 6 for MECE and SWE. We can see that although the field is oscillatory, the inclusion is identified as stiffer than the background in all experiments for both methods. In experiment 2, while both methods exhibit an increasing trend in the estimated modulus for areas near the push location, SWE presents a significantly higher deviation from the expected value for the inclusion (26.67 kPa) as compared to that obtained with MECE.

1. Statistics of shear modulus distribution

We computed the average shear modulus over inclusion and background within the computational domain shown in

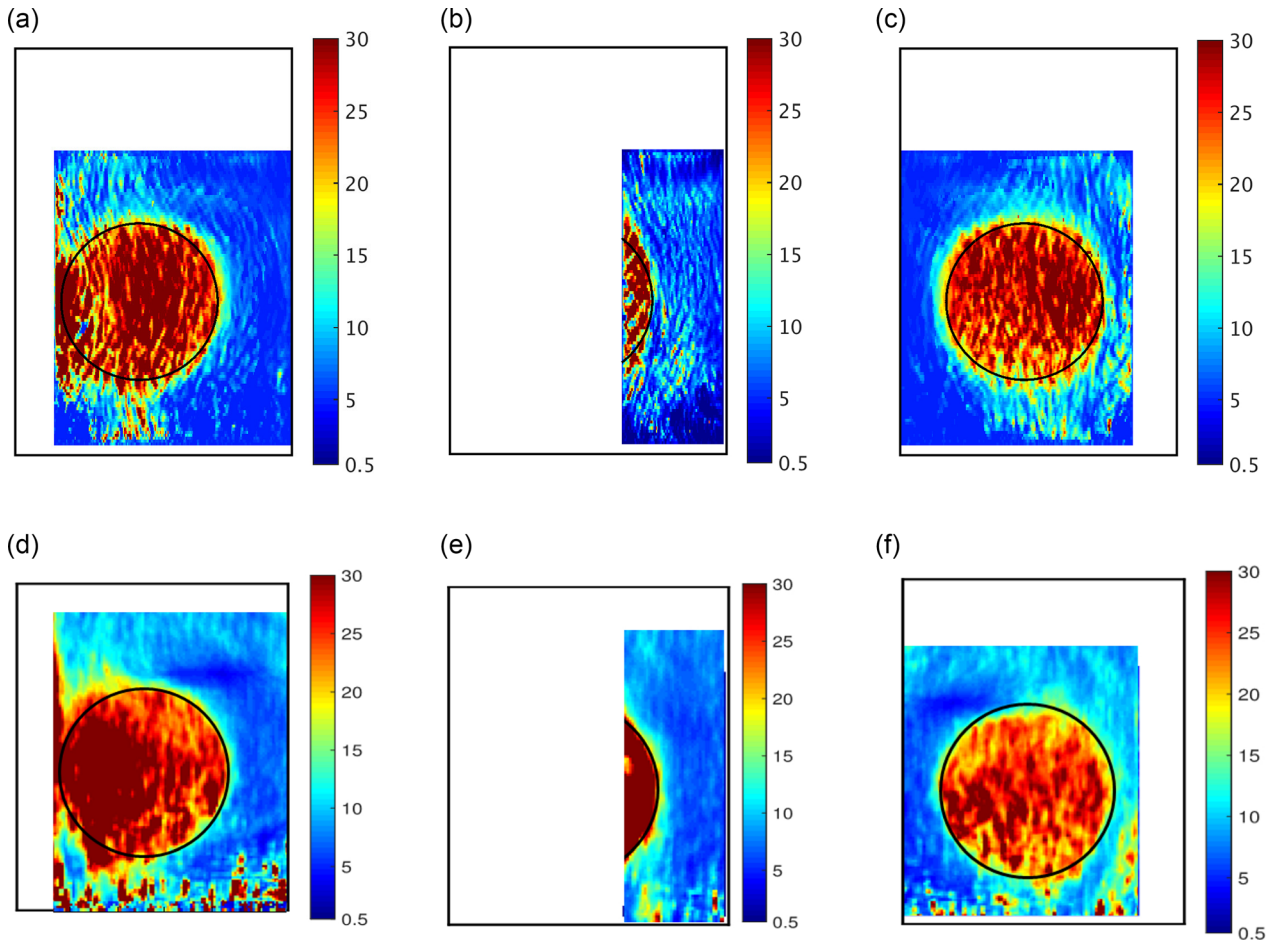

FIG. 7. (Color online) Reconstructed shear modulus distribution (in kPa) for experiments 1–3 using MECE and SWE. The solid line indicates the known location of the inclusion in the phantom. (a) MECE—experiment 1. (b) MECE—experiment 2. (c) MECE—experiment 3. (d) SWE—experiment 1. (e) SWE—experiment 2. (f) SWE—experiment 3.

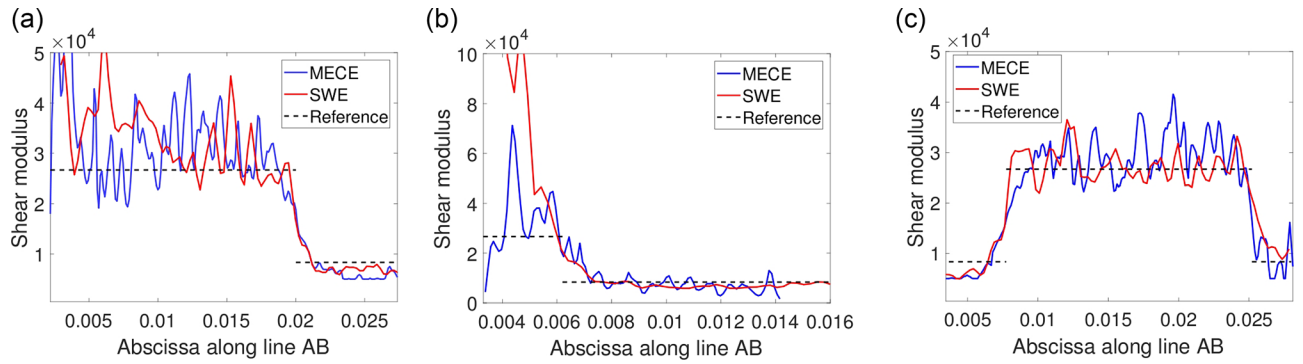

FIG. 8. (Color online) Reconstructed shear modulus distribution (in kPa) for experiments 1–3 using SWE and MECE. The dashed black line indicates the reference or known modulus value for the tissue mimicking phantom. (a) experiment 1. (b) experiment 2. (c) experiment 3.

Fig. 6 using MECE and SWE. These values are given in Table IV. In MECE, the average shear modulus of the background and that of the inclusion over the three experiments were 7.87 and 26.52 kPa, respectively. These values are in agreement with the already known values of the materials used in the experiments (8.33 and 26.67 kPa, respectively). Furthermore, the average values reported for the different experiments are consistent with each other. The observed variation in shear modulus is expected because of different levels of noise and modeling errors across different experiments.

SWE, in all three experiments, provided modulus values for the background material which were similar to those obtained with MECE and in good agreement with the known values from phantom descriptions. The estimated modulus of the inclusion from experiments 1 and 3 also presented acceptable bias and standard deviations. However, in experiment 2, a significant bias and standard deviation can be observed. The average of modulus values from all three experiments also show better agreement in the background compared to the inclusion.

VI. DISCUSSION AND SUMMARY

We have developed a full-wave inversion approach for reconstructing the elastic shear modulus distribution of a body from ARF-based experiments. The salient features of our proposed method are: (1) can handle complex wave propagation as it incorporates general governing equations as constraints, (2) can work with sparse data (e.g., unidirectional data), (3) subdomains with unknown boundary conditions are naturally handled, (4) no need to know sources and geometry in the forward problem. These features make our proposed method suitable for ultrasound-based imaging systems. We demonstrated the feasibility of the proposed approach using ultrasound experiments performed on a laboratory phantom. The phantom consisted of a soft matrix with a cylindrical inclusion. The main loading source in our experiments was the acoustic radiation force (ARF) at a particular location. The results show that the geometry of the inclusion was clearly identified in all experiments and the average shear modulus over the inclusion and background was accurately identified. In both simulated and phantom experiments, we also demonstrated the performance of a commonly used SWE reconstruction method. The quality of this reconstruction was highly dependent on geometry. SWE was shown to be able to closely capture the geometry of a cylindrical inclusion. In a triangular inclusion case, however, sharp edges were significantly distorted. The main speculation for this poor performance is strong violation of a plane wave propagation near abrupt modulus changes. The MECE approach, on the other hand, proved to be highly robust to geometry variations. In terms of accuracy in estimation of modulus, MECE was shown to provide values similar to known parameters in both simulated and phantom studies. SWE, on the other hand, showed sensitivity to both geometry changes as well as the location of reconstruction domain with regard to the radiation force location such that an increasingly positive bias was observed in the regions near the push location. We would like point out that our findings in terms of the performance of MECE with respect to SWE is still preliminary. A comprehensive comparison between the capabilities of these two methods requires further studies.

In summary, the proposed technique has potential for *in vivo* tissue characterization by offering versatility in the handling of waveforms, and flexibility in the selection of the domain of reconstruction by eliminating the requirement of boundary measurements.

Our future work will include adding a regularization term to the objective MECE functional in order to capture smoother shear modulus fields. Furthermore, we will perform validation studies for viscoelastic materials and perform *in vivo* experiments.

TABLE IV. Tissue mimicking phantom experiment: mean and standard deviation (STD) of shear modulus (in kPa) using a conventional SWE method and MECE.

	Background				Inclusion			
	SWE		MECE		SWE		MECE	
Experiment No.	Mean	STD	Mean	STD	Mean	STD	Mean	STD
1	8.72	3.03	7.58	2.67	28.31	7.75	26.22	4.92
2	8.72	35.73	7.95	2.28	55.25	57.00	26.99	14.4
3	9.51	3.17	8.08	2.67	23.33	5.19	26.35	5.67
Average of 1–3	8.98		7.87		36.21		26.52	
Actual	8.33		8.33		26.67		26.67	

ACKNOWLEDGMENTS

Research reported in this paper was supported by the National Cancer Institute of the National Institutes of Health under Award No. R01CA174723. The authors acknowledge the comments from Professor Azra Alizad of Mayo Clinic regarding the clinical relevance of ultrasound SWE.

APPENDIX

Using an identity tensor, $\mathbf{T}$, when measuring only vertical displacements is akin to assuming that the horizontal component of the computed displacement field is small when compared to the vertical components of the measured field. To see this, we decompose the measurement $\tilde{\boldsymbol{d}}$ into its contributions to the horizontal (e.g., $\tilde{d}_X$) and vertical directions (e.g., $\tilde{d}_Y$). We do the same for the computed displacements (i.e., u_X, u_Y). Then, since the horizontal displacements are not measured, we have $\tilde{d}_X = 0$ in the last term of the objective functional Eq. (3). Substituting these expressions into Eq. (3) yields

$$\Lambda(\boldsymbol{u}, \boldsymbol{\sigma}, G) := U(\boldsymbol{u}, \boldsymbol{\sigma}, G) + \frac{\kappa}{2}\int_{\Omega_m} \left(u_Y - \tilde{d}_Y\right)^2 + u_X^2 \, d\Omega.$$

Notice that the second term, which acts as a penalty term, enforces that the component u_X be small compared to the vertical component of the data. The first term enforces that the vertical component of the solution u_Y be close to the measured vertical displacements.

Aguilo, M., Aquino, W., Brigham, J., and Fatemi, M. (**2010**). "An inverse problem approach for elasticity imaging through vibroacoustics," IEEE Trans. Med. Imag. **29**, 1012–1021.

Albocher, U., Oberai, A., Barbone, P., and Harari, I. (**2009**). "Adjoint-weighted equation for inverse problems of incompressible plane-stress elasticity," Comput. Methods Appl. Mech. Eng. **198**, 2412–2420.

Arnal, B., Pinton, G., Garapon, P., Pernot, M., Fink, M., and Tanter, M. (**2013**). "Global approach for transient shear wave inversion based on the adjoint method: A comprehensive 2D simulation study," Phys. Med. Biol. **58**, 6765–6778.

Athanasiou, A., Tardivon, A., Tanter, M., Sigal-Zafrani, B., Bercoff, J., Diffieux, T., Gennisson, J., Fink, M., and Neuenschwander, S. (**2010**). "Breast lesions: Quantitative elastography with supersonic shear imaging—Preliminary results," Radiology **256**, 297–303.

Banerjee, B., Walsh, T., Aquino, W., and Bonnet, M. (**2013**). "Large scale parameter estimation problems in frequency-domain elastodynamics using an error in constitutive equation functional," Comput. Methods Appl. Mechan. Eng. **253**, 60–72.

Bayat, M., Denis, M., Gregory, A., Mehrmohammadi, M., Kumar, V., Meixner, D., Fazzio, R. T., Fatemi, M., and Alizad, A. (**2017**). "Diagnostic features of quantitative comb-push shear elastography for breast lesion differentiation," PLOS One **12**(3), e0172801.

Bercoff, J., Tanter, M., and Fink, M. (**2004**). "Supersonic shear imaging: A new technique for soft tissue elasticity mapping," IEEE Trans. Ultrason., Ferroelectr., Freq. Control **51**, 396–409.

Berg, W., Cosgrove, D., Dore, C., Schafer, F., Svensson, W., Hooler, R., Ohlinger, R., Mendelson, E., BaluMaestro, C., Locatelli, M., Tourasse, C., Cavanaugh, B., Juhan, V., Stavros, A., Tardivon, A., Gay, J., Henry, J., and Bacrie, C. (**2012**). "Shear-wave elastography improves the specificity of breast US: The BE1 multinational study of 939 masses," Radiology **262**, 435–449.

Brigham, J., Aquino, W., Mitri, F., Greenleaf, J., and Fatemi, M. (**2007**). "Inverse estimation of viscoelastic material properties for solids immersed in fluids using vibroacoustic techniques," J. Appl. Phys. **101**, 023509.

Cosgrove, D., Berg, W., Doré, C., Skyba, D., Henry, J., Gay, J., and Chen-Bacrie, C. (**2012**). "Shear wave elastography for breast masses is highly reproducible," Eur. Radiol. **22**, 1023–1032.

Denis, M., Gregory, A., Bayat, M., Fazzio, R. T., Whaley, D. H., Ghosh, K., Shah, S., Fatemi, M., and Alizad, A. (**2016**). "Correlating tumor stiffness with immunohistochemical subtypes of breast cancers: Prognostic value of comb-push ultrasound shear elastography for Differentiating luminal subtypes," PLOS One **11**(10), e0165003.

Diaz, M., Aquino, W., and Bonnet, M. (**2015**). "A modified error in constitutive equation approach for frequency-domain viscoelasticity imaging using interior data," Comput. Methods Appl. Mech. Eng. **296**, 129–149.

Doyley, M., Meaney, P., and Bamber, J. (**2000**). "Evaluation of an iterative reconstruction method for quantitative elastography," Phys. Med. Biol. **45**, 1521–1540.

Feissel, P., Olivier, A. (**2007**). "Modified constitutive relation error identification strategy for transient dynamics with corrupted data: The elastic case," Comput. Methods Appl. Mech. Eng. **196**, 1968–1983.

Krouskop, T., Dougherty, D., and Vinson, F. (**1987**). "A pulsed Doppler ultrasonic system for making noninvasive measurements of the mechanical properties of soft tissue," J. Rehabil. Res. **24**, 1–8.

Laurent, S., Tanter, M., Catheline, S., and Fink, M. (**2002**). "Shear modulus imaging with 2-D transient elastography," IEEE Trans. Ultrason., Ferroelectr., Freq. Control **49**, 426–435.

Loupas, T., and Powers, J. (**1995**). "An axial velocity estimator for ultrasound blood flow imaging, based on a full evaluation of the Doppler equation by means of a two-dimensional autocorrelation approach," IEEE Trans. Ultrason., Ferroelectr., Freq. Control **42**, 672–688.

Muthupillai, R., Lomas, D., Rossman, P., Greenleaf, J., Manduca, A., and Ehman, R. (**1995**). "Magnetic resonance elastography by direct visualization of propagating acoustic strain waves," Science **269**, 1854–1857.

Nightingale, K., McAleavey, S., and Trahey, G. (**2003**). "Shear-wave generation using acoustic radiation force: *In vivo* and *ex vivo* results," Ultrasound Med. Biol. **29**, 1715–1723.

Oberai, A., Gokhale, N., and Feijóo, G. (**2003**). "Solution of inverse problems in elasticity imaging using the adjoint method," Inverse Probl. **19**, 297–313.

Oliphant, T., Manduca, A., Ehman, R., and Greenleaf, J. (**2001**). "Complex-valued stiffness reconstruction for magnetic resonance elastography by algebraic inversion of the differential equation," Mag. Reson. Med. **45**, 299–310.

Ophir, J., Céspedes, I., Ponnekanti, H., Yazdi, Y., and Li, X. (**1991**). "Elastography: A quantitative method for imaging the elasticity of biological tissues," Ultrason. Imag. **13**, 111–134.

Park, E., Maniatty, A. (**2006**). "Shear modulus reconstruction in dynamic elastography: Time harmonic case," Phys. Med. Biol. **51**, 3697–3721.

Sinkus, R., Tanter, M., Catheline, S., Lorenzen, J., Kuhl, C., Sondermann E., and Fink, M. (**2005**). "Imaging anisotropic and viscous properties of breast tissue by magnetic resonance-elastography," Mag. Reson. Med. **53**, 372–387.

Song, P., Manduca, A., Zhao, H., Urban, M., Greenleaf, J., and Chen, S. (**2014**). "Fast shear compounding using robust 2-D shear wave speed calculation and multi-directional filtering," Ultrasound Med. Biol. **40**, 1343–1355.

Song, P., Zhao, H., Manduca, A., Urban, M., Greenleaf, J., and Chen, S. (**2012**). "Comb-Push Ultrasound Shear Elastography (CUSE): A Novel Method for Two-Dimensional Shear Elasticity Imaging of Soft Tissues," IEEE Trans. Med. Imag. **31**, 1821–1832.

Warner, J., Diaz, M., Aquino, W., and Bonnet, M. (**2014**). "Inverse material identification in coupled acoustic-structure interaction using a modified error in constitutive equation functional," Comput. Mech. **54**, 645–659.

Zhao, H., Song, P., Urban, M., Kinnick, R., Yin, M., Greenleaf, J., and Chen, S. (**2011**). "Bias observed in time-of-flight shear wave speed measurements using radiation force of a focused ultrasound beam," Ultrasound Med. Biol. **37**, 1884–1892.